

Electronic Supplementary Information (ESI) for

**Rational design of a phenothiazine-based donor-acceptor covalent
organic framework for enhanced photocatalytic oxidative coupling of
amines and cyclization of thioamides**

Yang Liu,^a Xinyue Jiang,^a Likun Chen,^b Yan Cui,^b Qiu-Yan Li,^{*a} Xinsheng Zhao,^a Xiguang Han,^a
Yong-Chao Zheng^{*b} and Xiao-Jun Wang^{*a}

^a*Jiangsu Key Laboratory of Green Synthetic Chemistry for Functional Materials, School of
Chemistry and Materials Science, School of Physics and Materials Science, Jiangsu Normal
University, Xuzhou 221116, P. R. China. E-mail: xjwang@jsnu.edu.cn; qyli@jsnu.edu.cn*

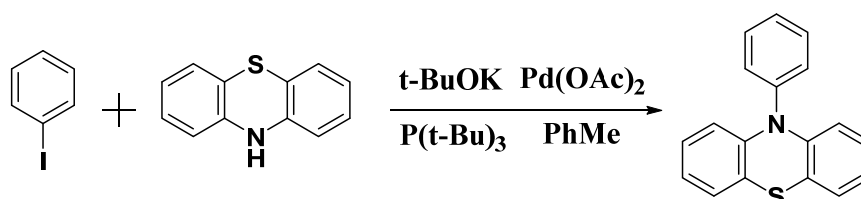
^b*State Key Laboratory of NBC Protection for Civilian, Beijing, 102205, PR China. E-mail:
zhengycfh@163.com*

General method and materials

Unless specifically mentioned, all chemicals are commercially available and were used as received. ^1H and ^{13}C NMR spectra were taken on a Bruker AV400 at room temperature. High-resolution mass spectrometry (HR-MS) was performed on a Thermo ultimate Q-Exactive in positive mode. ^{13}C cross-polarization/magic angle spinning solid-state nuclear magnetic resonance (CP/MAS ssNMR) experiments were performed on a Bruker AVANCE III 400 WB spectrometer operating at 100.62 MHz for ^{13}C using a double resonance 4 mm MAS NMR probe and a sample spinning rate of 6 kHz. The powder X-ray diffraction measurements were taken on a Bruker D8 diffractometer using Cu-K_α radiation ($\lambda = 1.5418 \text{ \AA}$) at room temperature. Low-pressure gas sorption measurements were performed by using Quantachrome Instruments Autosorb-iQ with the extra-high pure gases. Brunauer-Emmett-Teller (BET) surface area and pore size distribution were calculated from the N_2 sorption isotherms at 77 K based on the solid density functional theory (QSDFT) model in the Quantachrome ASiQwin 2.01 software package. UV-vis diffuse reflectance spectra (UV-vis DRS) were recorded at room temperature on an Agilent Cary 7000 Spectrophotometer. Photoluminescence (PL) spectra were obtained with an Edinburgh FLS920 spectrophotometer. The infrared spectra were recorded on a Thermo Scientific Nicolet iS10 FT-IR spectrometer as KBr pellets. Temperature-dependent photoluminescence spectra were recorded on a HORIBA FluoroMax Plus module fluorescence spectrometer. ESR spectra were recorded at room temperature using a Bruker A300 spectrometer at 9.8 GHz, X-band, with 100 Hz field modulation. Ultraviolet photoelectron spectroscopy (UPS) and X-ray photoelectron spectroscopy (XPS) were performed on Thermo Scientific Escalab 250Xi and K-Alpha. Field-emission scanning electron microscopy (FE-SEM) images were obtained on a HITACHI S-8010 instrument operating at 10 kV. Transmission electron microscopy (TEM) images were obtained on a JEM 2100F operating at 200 kV.

Synthesis and Characterizations

10-phenyl-10H-phenothiazine (PTZ):



Toluene (100 mL) was added to a 250 mL two-necked flask and nitrogen was used to degas it for two hours. After the previous step was completed 10H-phenothiazine (4.98 g, 25.0 mmol), iodobenzene (6.12 g, 30.0 mmol), potassium *t*-butoxide (4.20 g, 37.5 mmol), $\text{Pd}(\text{OAc})_2$ (280 mg, 1.3 mmol), and *tert*-butyl phosphate ($\text{P}(\text{t-Bu})_3$) (1.26 g, 6.3 mmol) was added to the reaction flask, and evacuated and filled with nitrogen three times. The mixture was stirred and then heated at 110 °C for 24 h. After that, the mixture was poured into ice water and then was extracted with DCM; the combined organic layers were dried over anhydrous Na_2SO_4 and filtered. The solvent was removed under rotary evaporation. The product was purified by column chromatography over a silica gel column using petroleum ether-ethyl acetate (v/v, 60/1) to give a white solid (5.53 g, 20.1 mmol, yield: 80%). ^1H NMR (400 MHz, d_6 -DMSO) δ 7.67 (t, $J = 7.6$ Hz, 2H), 7.54 (t, $J = 7.3$ Hz, 1H), 7.42 (d, $J = 7.9$ Hz, 2H), 7.08 (d, $J = 7.4$ Hz, 2H), 6.89 (dt, $J = 29.0, 7.3$ Hz, 4H), 6.16 (d, $J = 8.1$ Hz, 2H).

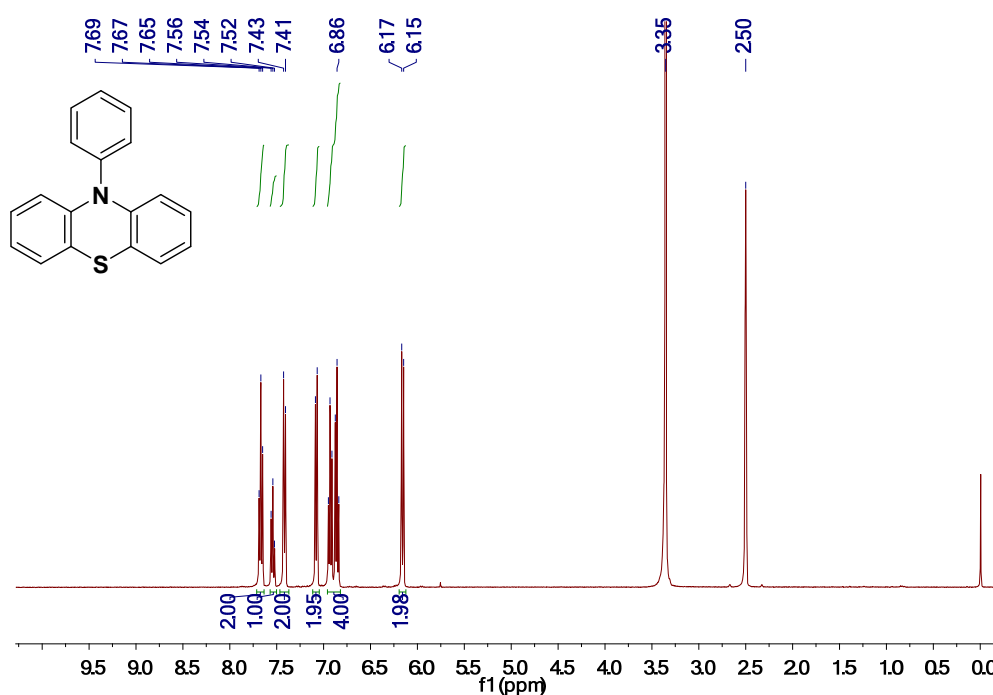
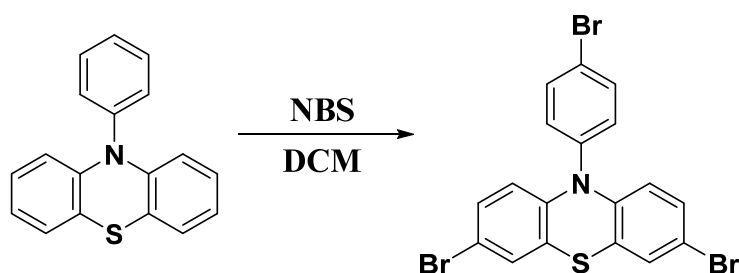


Fig. S1. ^1H NMR of compound PTZ (400 MHz, d_6 -DMSO).

3,7-dibromo-10-(4-bromophenyl)-10H-phenothiazine (PTZ-3Br):



To a mixture of 10-phenyl-10H-phenothiazine (3.99 g, 14.5 mmol) in DCM (80 mL), N-bromosuccinimide (8.53 g, 47.9 mmol) was added into the above mixture in batches. The mixture was stirred at room temperature for 12 h. After that, the mixture was poured into ice water and extracted with DCM and the combined organic extracts were dried over anhydrous Na_2SO_4 and concentrated. The crude product was purified by column chromatography over a silica gel column using petroleum ether and dichloromethane (v/v, 10/1) to give a white solid (6.38 g, 12.5 mmol, yield: 86%). ^1H NMR (400 MHz, d_6 -DMSO) δ 7.86 (d, $J = 8.2$ Hz, 2H), 7.40 (d, $J = 8.3$ Hz, 2H), 7.31 (s, 2H), 7.15 – 7.04 (m, 2H), 6.05 (d, $J = 8.8$ Hz, 2H).

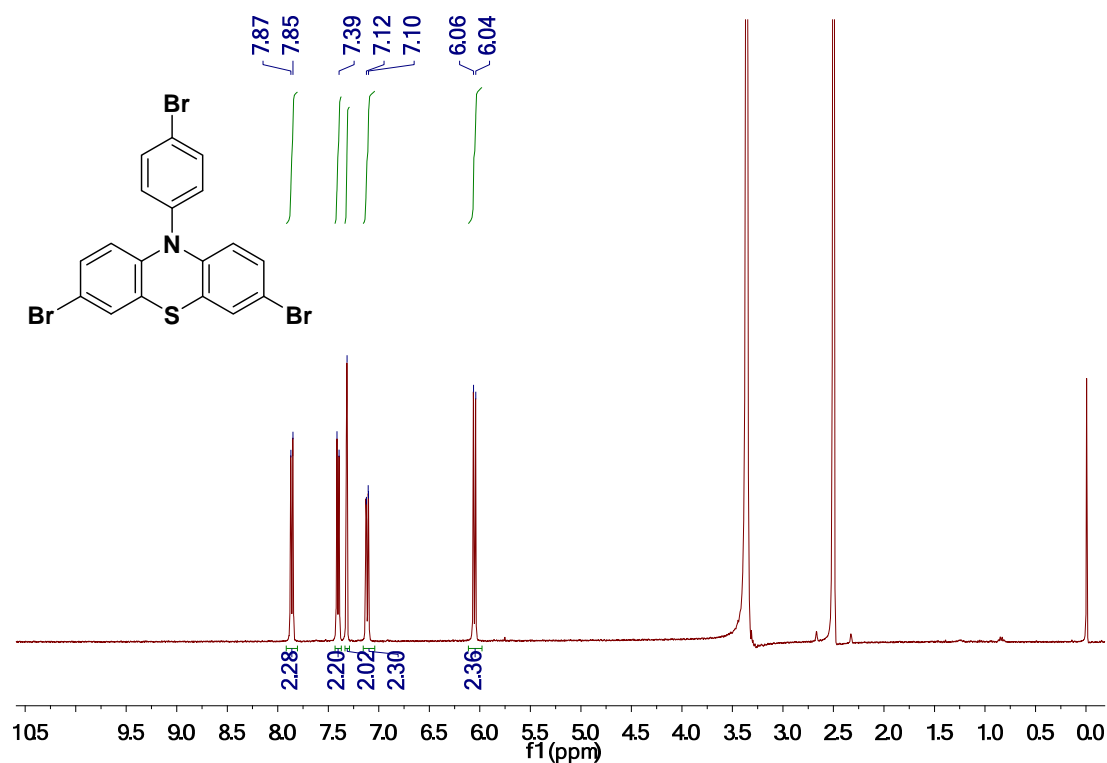
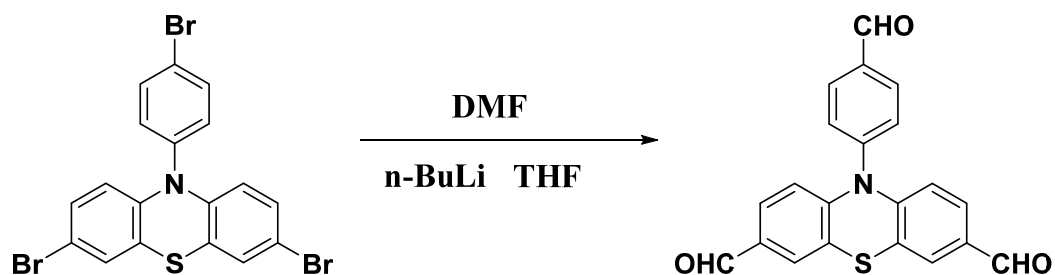


Fig. S2 ^1H NMR of compound PTZ-3Br (400 MHz, d_6 -DMSO).

10-(4-formylphenyl)-10H-phenothiazine-3,7-dicarbaldehyde (PTZ-CHO):



In a 250 mL two-neck flask, the suspension of 3,7-dibromo-10-(4-bromophenyl)-10H-phenothiazine (3.53 g, 6.9 mmol) in dry THF (100 ml) was cooled down to -78 °C under N₂ condition and then the solution of *n*-BuLi (28 mL, 69.9 mmol, 2.5 M in hexane) was added. The mixture was stirred at -78 °C for 1 h and then dry DMF (4.47 g, 62.1 mmol) was added. The reaction was at the same temperature for one hour, and restoration of room temperature. The reaction system was extracted with ethyl acetate and an appropriate amount of hydrochloric acid was added. Wash the organic phase with saturated salt water to pH = 7. The combined organic extracts were dried over anhydrous Na₂SO₄ and concentrated to obtain an orange solid. The crude product was purified by column chromatography over a silica gel column using dichloromethane and ethyl acetate (v/v, 20/1) to give an orange solid (1.73 g, 4.8 mmol, yield: 70%). ¹H NMR (400 MHz, *d*₆-DMSO) δ 10.17 (s, 1H), 9.75 (s, 2H), 8.26 (d, *J* = 8.0 Hz, 2H), 7.79 (d, *J* = 8.0 Hz, 2H), 7.60 (s, 2H), 7.46 (d, *J* = 8.6 Hz, 2H), 6.22 (d, *J* = 8.5 Hz, 2H). ¹³C NMR (CDCl₃, 101 MHz) δ 190.80, 189.72, 146.99, 144.81, 136.91, 132.83, 132.49, 131.42, 130.04, 127.88, 120.66, 116.20, EI-HRMS: *m/z* calcd for C₂₁H₁₃NO₃S: 359.0616, found: 359.0608 [M]⁺.

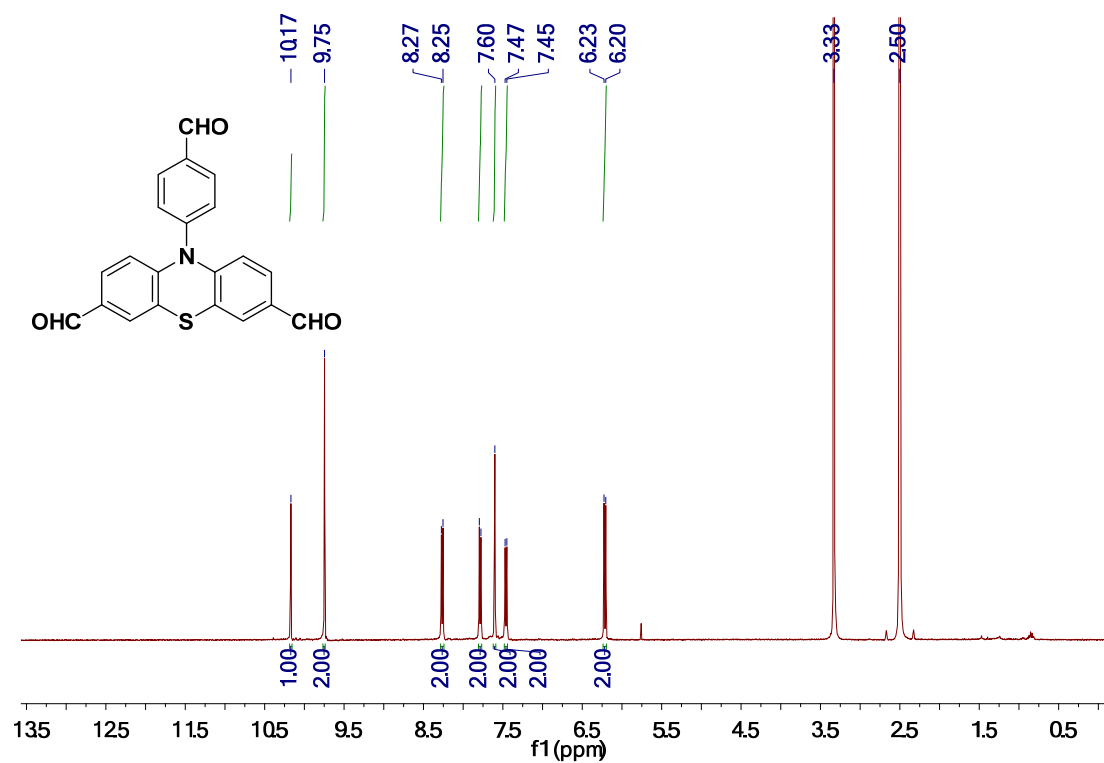


Fig. S3 $^1\text{H NMR}$ of compound PTZ-CHO (400 MHz, d_6 -DMSO).

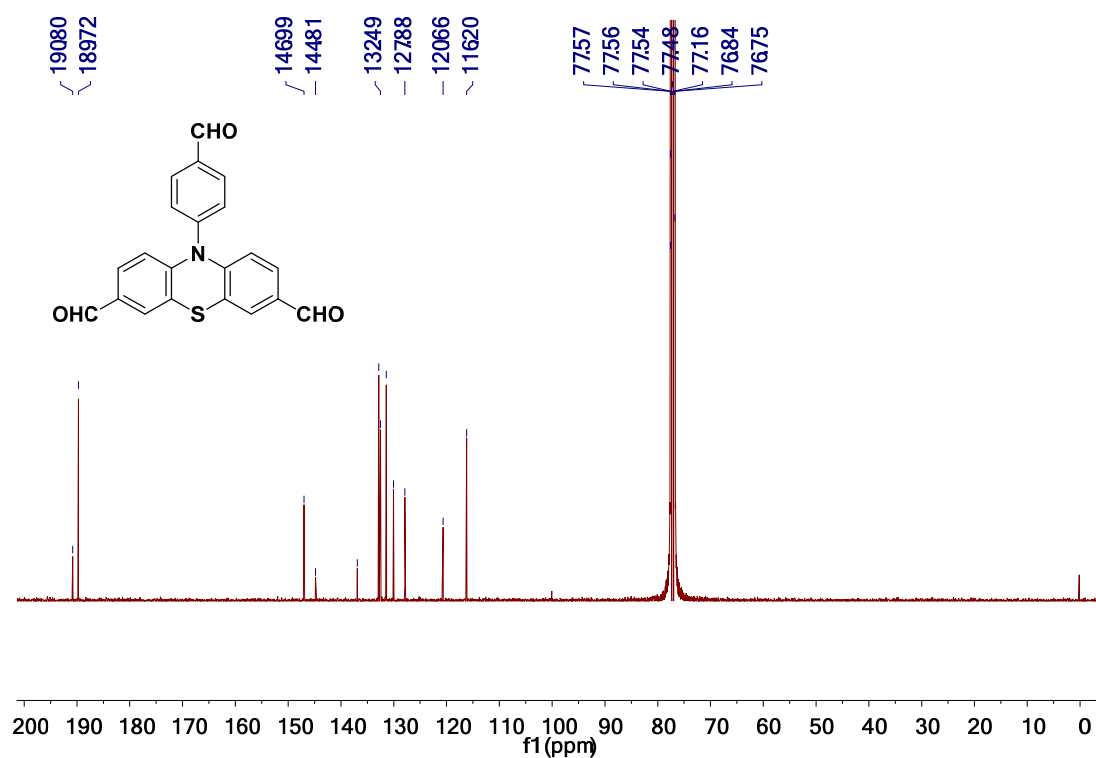


Fig. S4. $^{13}\text{C NMR}$ of compound PTZ-CHO (101 MHz, CDCl_3).

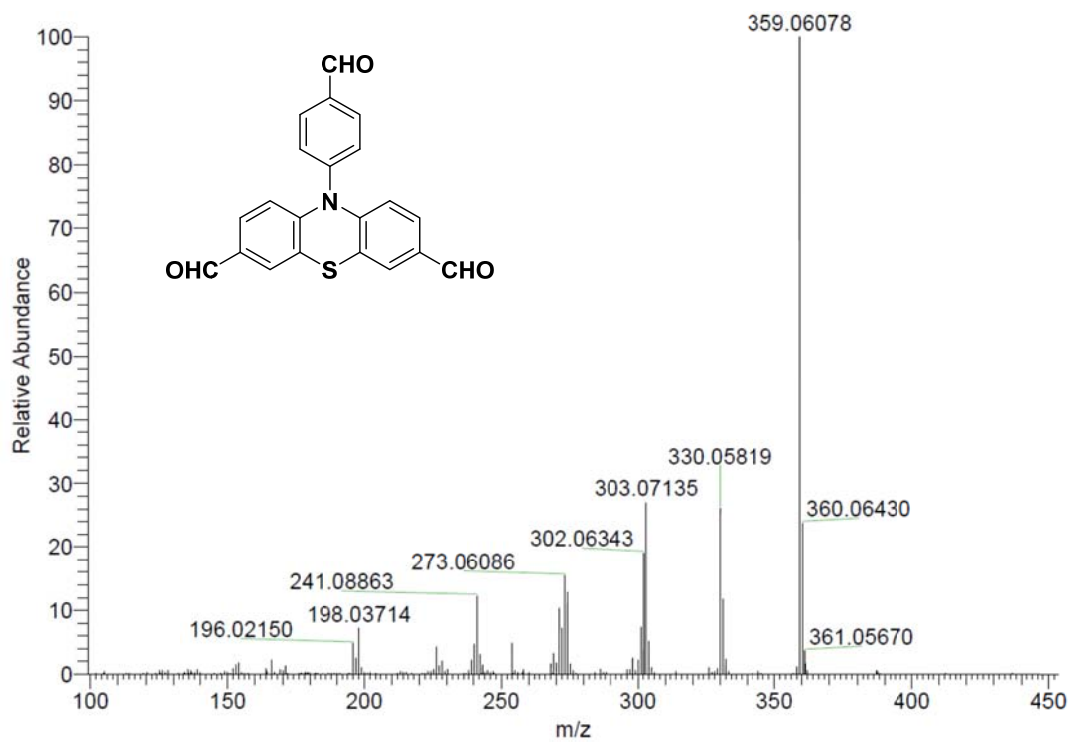
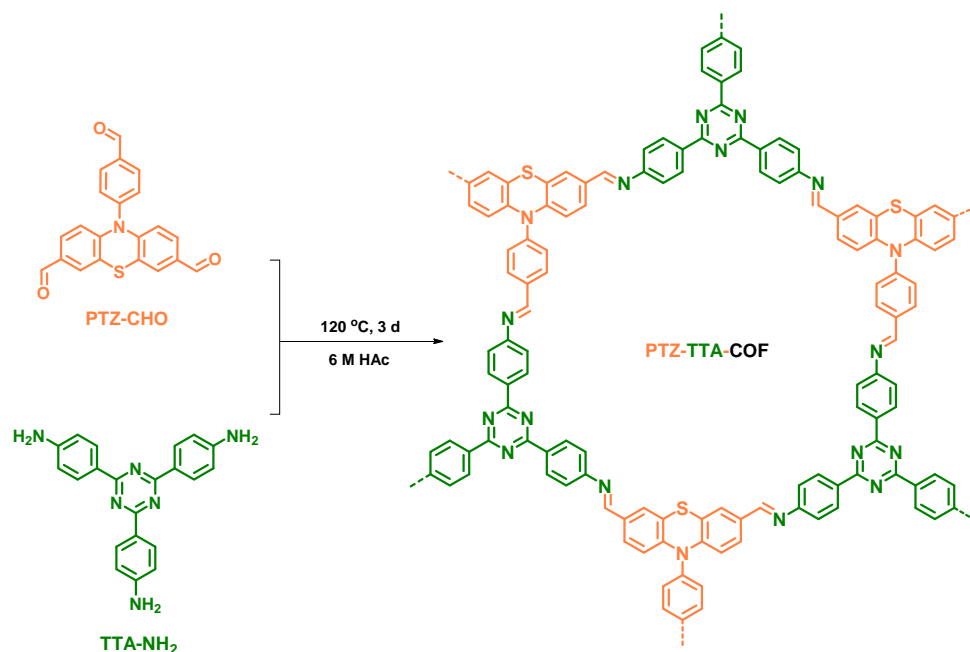


Fig. S5. EI-HRMS spectrum of compound **PTZ-CHO**.

Synthesis of PTZ-TTA-COF



A mixture of TTA-NH₂ (21 mg, 0.06 mmol), PTZ-CHO (21 mg, 0.056 mmol), acetic acid (6 M, 0.1 mL) in *o*-dichlorobenzene (*o*-DCB)/diphenyl ether (DPE) (0.3 mL/0.7 mL) in a Pyrex tube (5 mL) was first sonicated for 30 minutes and then flash frozen at 77 K (liquid N₂ bath) and degassed by three times of freeze-pump-thaw cycle. The tube was sealed off under a flame and then heated at 120 °C for 72 h. After cooling to room temperature, the red precipitate was washed several times until the upper layer is colorless with THF, MeOH, and acetone, respectively. The resulting powder was subjected to Soxhlet extraction with THF for 12 h, and then dried under vacuum at 60 °C overnight to obtain a bright red solid (80%).

Table S1. Optimization of synthetic conditions for **PTZ-TTA-COF**.

Entry	Solvents	T (°C)	Crystallinity	Yield
1	Mesitylene/Dioxane/6M HAc = 0.3/0.7/0.1	120	low	low
2	Mesitylene/Dioxane/6M HAc = 0.5/0.5/0.1	120	low	low
3	Mesitylene/Dioxane/6M HAc = 0.7/0.3/0.1	120	No	low
4	Mesitylene/Butanol/6M HAc = 0.3/0.7/0.1	120	No	No
5	Mesitylene/Butanol/6M HAc = 0.5/0.5/0.1	120	No	No
6	Mesitylene/Butanol/6M HAc = 0.7/0.3/0.1	120	No	No
7	Mesitylene/Butanol/6M HAc = 0.7/0.3/0.1	80	Moderate	low
8	Mesitylene/Butanol/HAc = 0.3/0.7/0.1	80	low	low
9	Mesitylene/Butanol/HAc = 0.7/0.3/0.1	80	High	low
10	Mesitylene/DPE/6M HAc = 0.7/0.3/0.1	120	High	High
11	Mesitylene/DPE/6M HAc = 0.3/0.7/0.1	120	High	High
12	Mesitylene/DPE/6M HAc = 0.7/0.3/0.1	150	High	High
13	Mesitylene/DPE/6M HAc = 0.3/0.7/0.1	150	High	High
14	Mesitylene/DPE/12M HAc = 0.7/0.3/0.1	120	High	High
15	Mesitylene/DPE/12M HAc = 0.5/0.5/0.1	120	High	High
16	Mesitylene/DPE/12M HAc = 0.3/0.7/0.1	120	High	High
17	<i>o</i> -DCB/DPE/6M HAc = 0.7/0.3/0.1	120	High	High
18	<i>o</i> -DCB/DPE/6M HAc = 0.5/0.5/0.1	120	High	High
19	<i>o</i> -DCB/DPE/6M HAc = 0.3/0.7/0.1	120	Highest	High
20	<i>o</i> -DCB/DPE/12M HAc = 0.7/0.3/0.1	150	Highest	High
21	Butanol/DPE/12M HAc = 0.7/0.3/0.1	120	Highest	High
22	CH ₃ CN/HAc = 1/0.05	RT	No	Moderate
23	CH ₃ CN/12M HAc = 1/0.1	RT	No	Moderate
24	Mesitylene/DPE/6M HAc = 0.5/0.5/0.1	RT	Moderate	Moderate
25	Mesitylene/DPE/12M HAc = 0.5/0.5/0.05	RT	High	Moderate

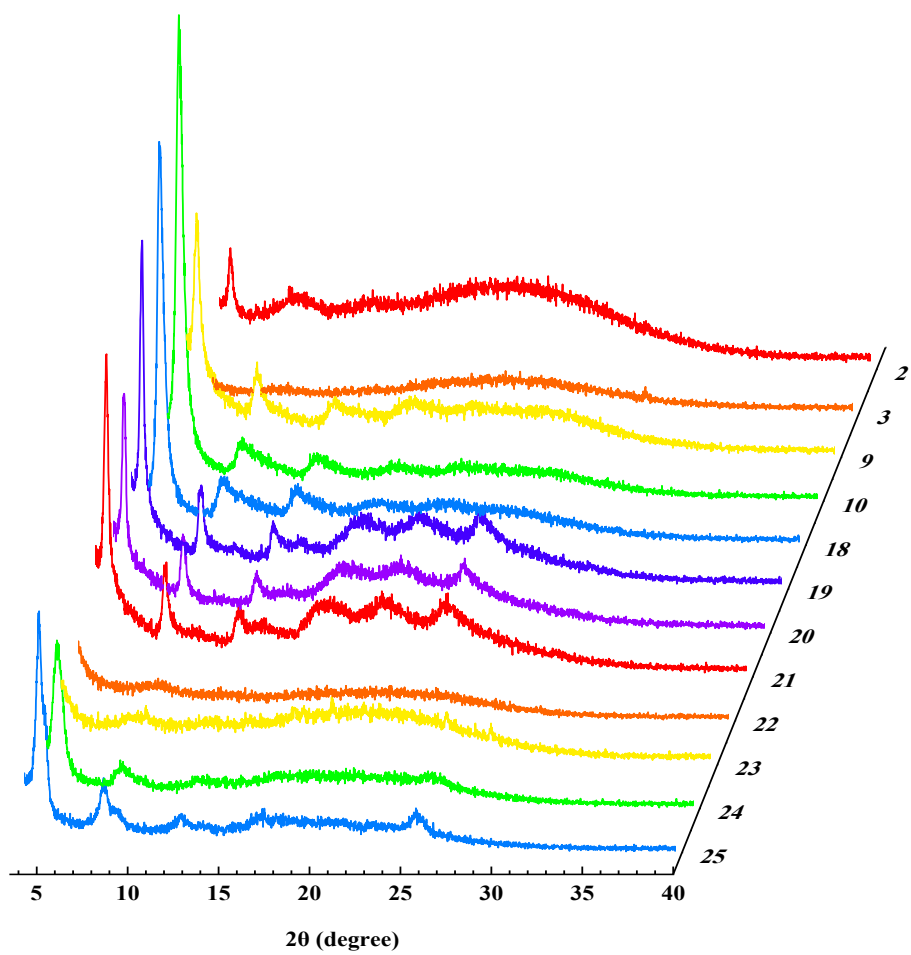


Fig. S6 PXRD patterns of representative PTZ-TTA-COF samples in Table S1.

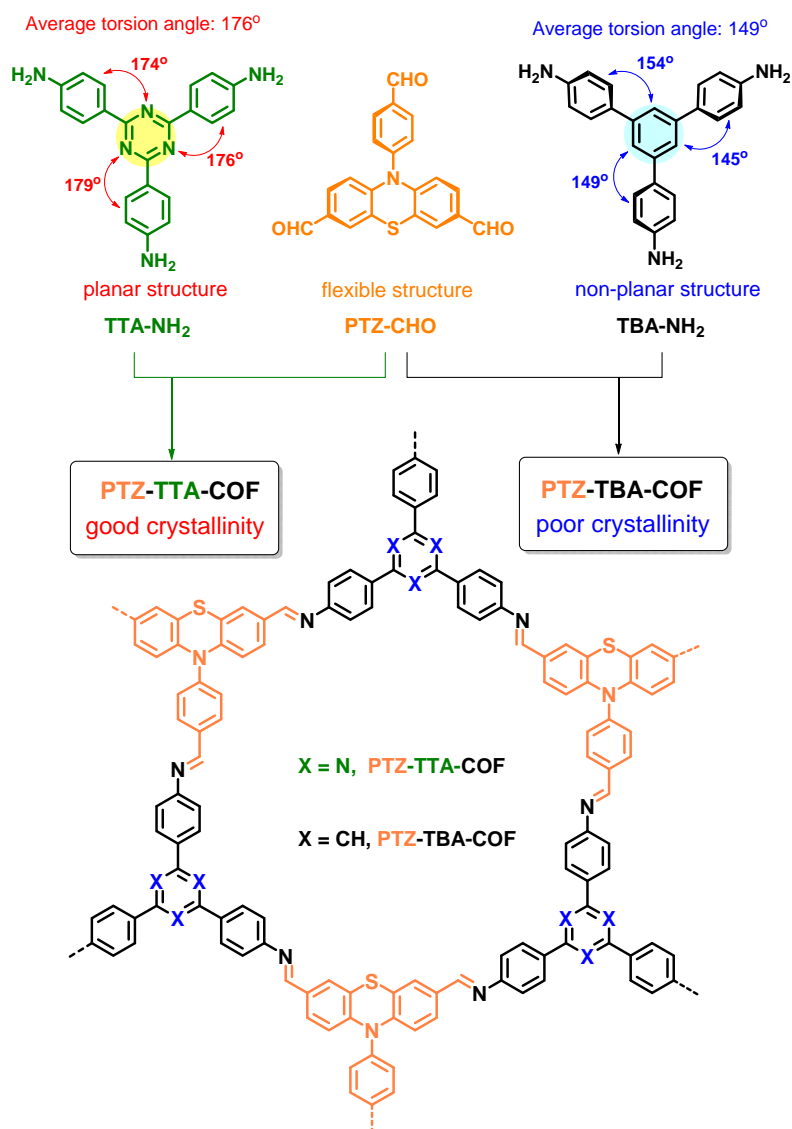


Fig. S7 The torsion angle comparison of TTA-NH₂ and TBA-NH₂ amine building blocks as well as the chemical structures of corresponding COFs. The PTZ-TBA-COF was synthesized by the similar procedure as PTZ-TTA-COF.

The torsion angle data was taken from the literature report.^{S1} It can be found that the three phenyl rings connected to the central triazine core in TTA-NH₂ are almost in the same plane, whereas for TBA-NH₂, the central triphenyl cores are not in the same plane due to the steric interactions among the *ortho* hydrogens. As a consequence, the resulting PTZ-TTA-COF exhibited a much better crystallinity than that of PTZ-TBA-COF under the assistance of TTA-NH₂ with a

more planar structure, as evidenced by their PXRD patterns (**Fig. S8**). This result revealed that the planar structure of TTA-NH₂ played an important role in crystallizing flexible PTZ unit into a COF framework. Besides, the PTZ unit adopted a typical butterfly shaped configuration in COF lattice with a dihedral angle of 147°, which is quite different from the PTZ-CHO monomer (**Fig. S9** and **Fig. S10**). Such confirmation allows for the COF layer stacking, while the average interlayer distance is around 3.6 Å that is a little larger than the distance of 3.3-3.5 Å in common COFs, due to the butterfly configuration of PTZ subunit in PTZ-TTA-COF.

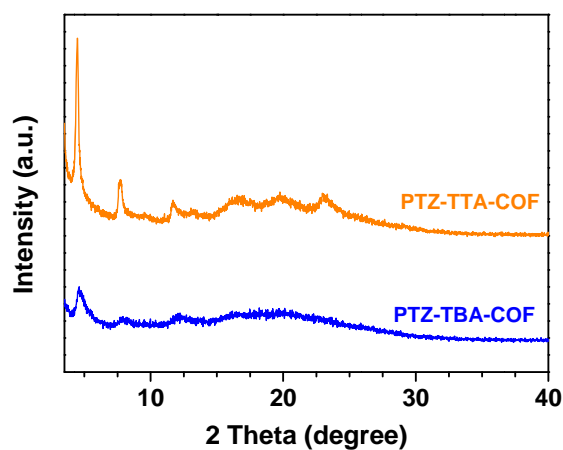


Fig. S8 PXRD patterns of PTZ-TTA-COF and PTZ-TBA-COF. It is clear that PXRD peaks of the control PTZ-TBA-COF are weak and broad, suggesting its poor crystallinity due to the non-planar structure of TBA-NH₂.

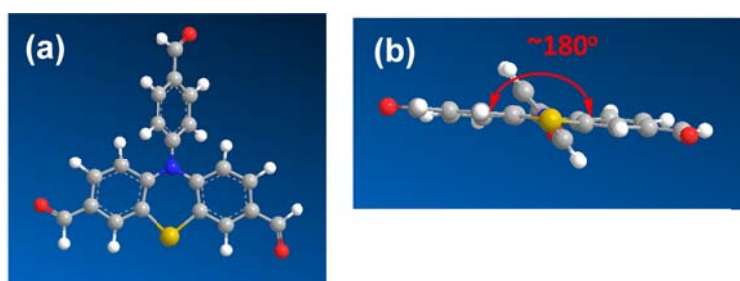


Fig. S9 The optimized structure of PTZ-CHO monomer in top (a) and side (b) view, indicative of its non-planar structure.

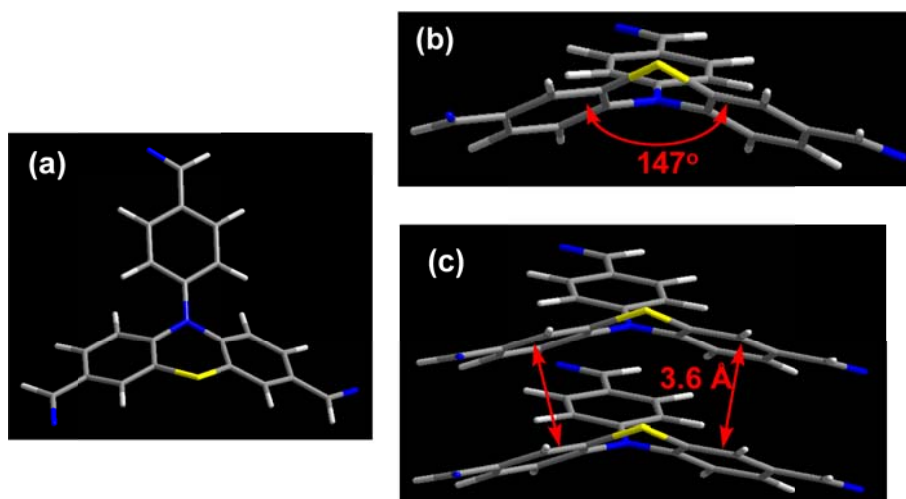


Fig. S10 The optimized structure of PTZ part in COF framework from top (a), side (b) and packing (c) view, showing that the three phenyl rings are also not in the same plane. In contrast to PTZ-CHO monomer, the PTZ unit adopted a typical butterfly shaped configuration in PTZ-TTA-COF lattice, on account of its flexible and variable confirmation. The dihedral angle for two benzene rings in PTZ is about 147°. And the distance of the two layers is 3.6 Å that is a little larger than the distance of 3.3-3.5 Å in common COFs, due to the butterfly configuration of PTZ subunit in PTZ-TTA-COF.

Synthesis of PTZ-TBA-COF

The PTZ-TBA-COF was synthesized by the similar procedure as PTZ-TTA-COF. Specifically, a mixture of TBA-NH₂ (21 mg, 0.06 mmol), PTZ-CHO (21 mg, 0.056 mmol), acetic acid (6 M, 0.1 mL) in *o*-dichlorobenzene (*o*-DCB)/diphenyl ether (DPE) (0.5 mL/0.5 mL) in a Pyrex tube (5 mL) was first sonicated for 30 minutes and then flash frozen at 77 K (liquid N₂ bath) and degassed by three times of freeze-pump-thaw cycle. The tube was sealed off under a flame and then heated at 120 °C for 72 h. After cooling to room temperature, the orange precipitate was washed several times until the upper layer is colorless with THF, MeOH, and acetone, respectively. The resulting powder was subjected to Soxhlet extraction with THF for 12 h, and then dried under vacuum at 60 °C overnight to obtain orange solid (76%).

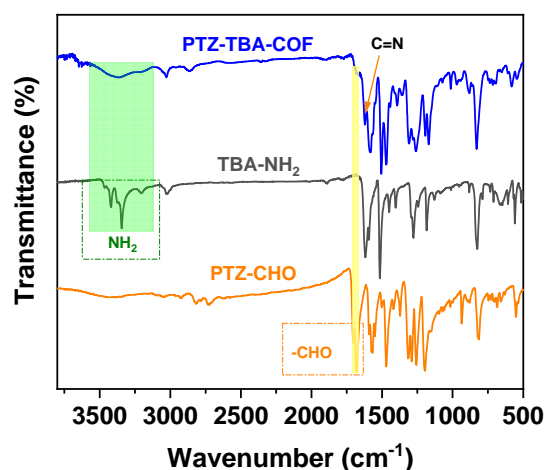


Fig. S11 FT-IR spectra of PTZ-CHO, TBA-NH₂ and PTZ-TBA-COF. It can be observed that stretching bands of CHO and NH₂ in monomers are almost disappeared in COF sample, while a characteristic signal of C=N stretching peak at 1623 cm⁻¹ is detected in PTZ-TBA-COF sample. This FT-IR comparison confirmed the formation of imine-bridged framework structure with the high polycondensation degree of amine and aldehyde precursors in PTZ-TBA-COF.

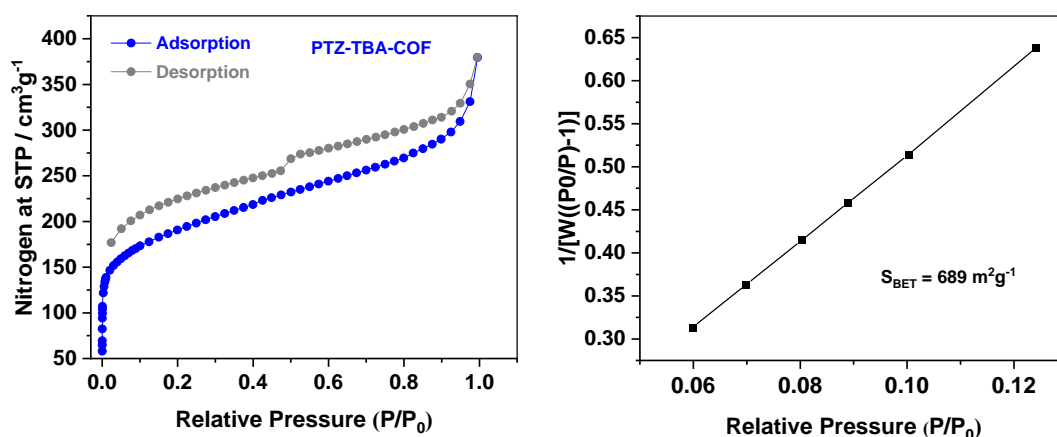


Fig. S12 Nitrogen sorption isotherm at 77K (left) and BET specific surface area plot (right) for PTZ-TBA-COF, confirming its good porosity.

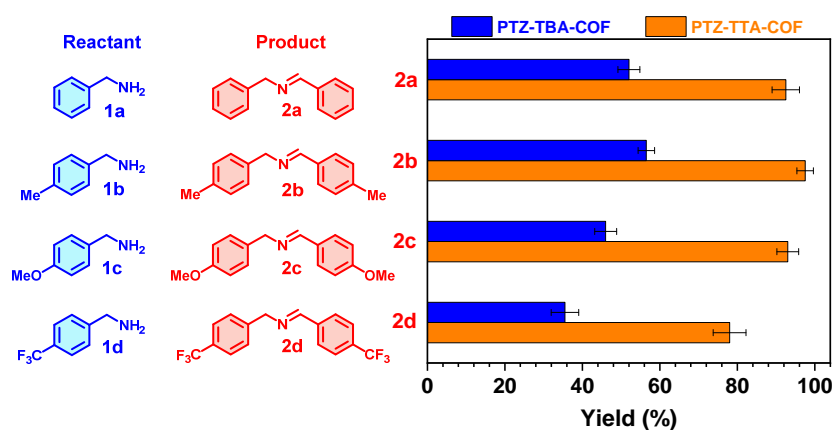
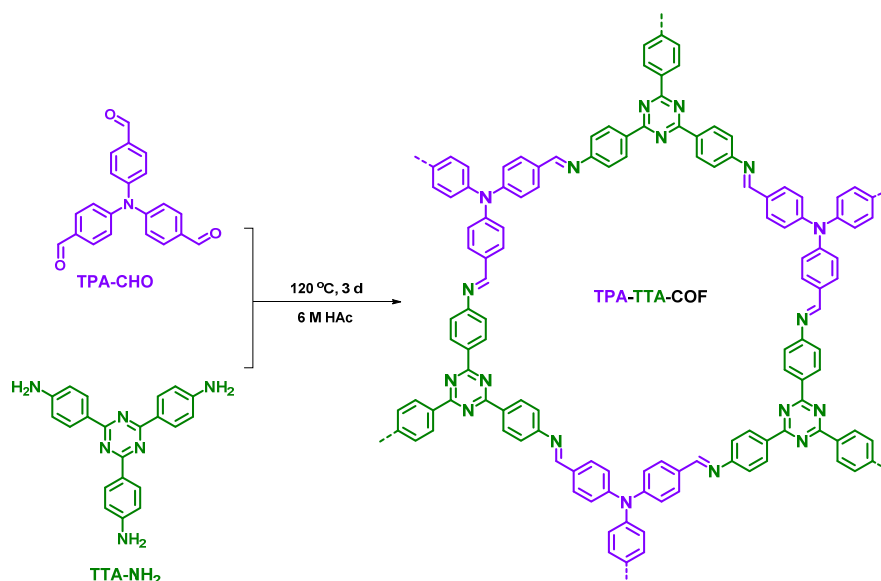


Fig.S13 Comparison of PTZ-TTA-COF and PTZ-TBA-COF for photocatalyzing oxidative coupling of four benzylamines into imines at room temperature under air. Reaction conditions: amine (0.1 mmol), COF photocatalyst (2 mg), CD₃CN (1 mL), blue LEDs ($\lambda_{\max} = 450$ nm, 3 W x 4), 1 h. The yields were determined by ¹H NMR.

As for the two COFs, the donor parts are the same PTZ unit, while the TBA unit is a weaker acceptor in relative to TTA unit. As a result, the stronger D-A interaction is expected for PTZ-TTA-COF in comparison to PTZ-TBA-COF. Thus, PTZ-TTA-COF exhibited higher photocatalytic activities than PTZ-TBA-COF under the same reaction conditions

Synthesis of TPA-TTA-COF



The control TPA-TTA-COF with the similar hexagonal reticular structure but small D-A contrast was prepared according to the previous reports and its PXRD pattern was consistent with the reported one.^{S2-S4} A mixture of TTA-NH₂ (21 mg, 0.06 mmol), TPA-CHO (20 mg, 0.06 mmol), and acetic acid (6 M, 0.1 mL) in 1,4-dioxane/*o*-dichlorobenzene (*o*-DCB) (0.5 mL/0.5 mL) in a Pyrex tube (5 mL) was first sonicated for 30 minutes and then flash frozen at 77 K (liquid N₂ bath) and degassed by three times of freeze-pump-thaw cycles. The tube was sealed off under a flame and then heated at 120 °C for 72 h. After that cooling to room temperature, the yellow precipitate was washed several times with THF, MeOH, and acetone, respectively, and then dried under vacuum at 120 °C overnight to obtain a yellow solid (82%).

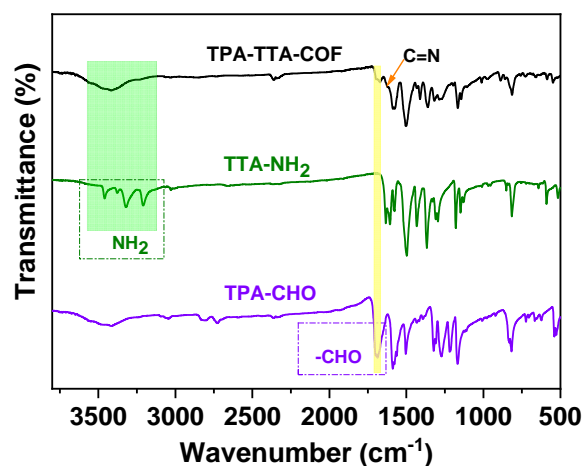


Fig. S14 FT-IR spectra of TPA-CHO, TTA-NH₂ and TPA-TTA-COF.

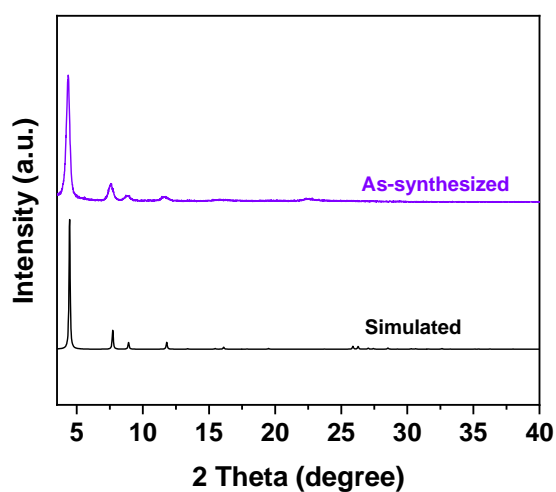


Fig. S15 The comparison for simulated and as-synthesized PXRD patterns of TPA-TTA-COF, identifying its AA stacking mode and crystalline structure.

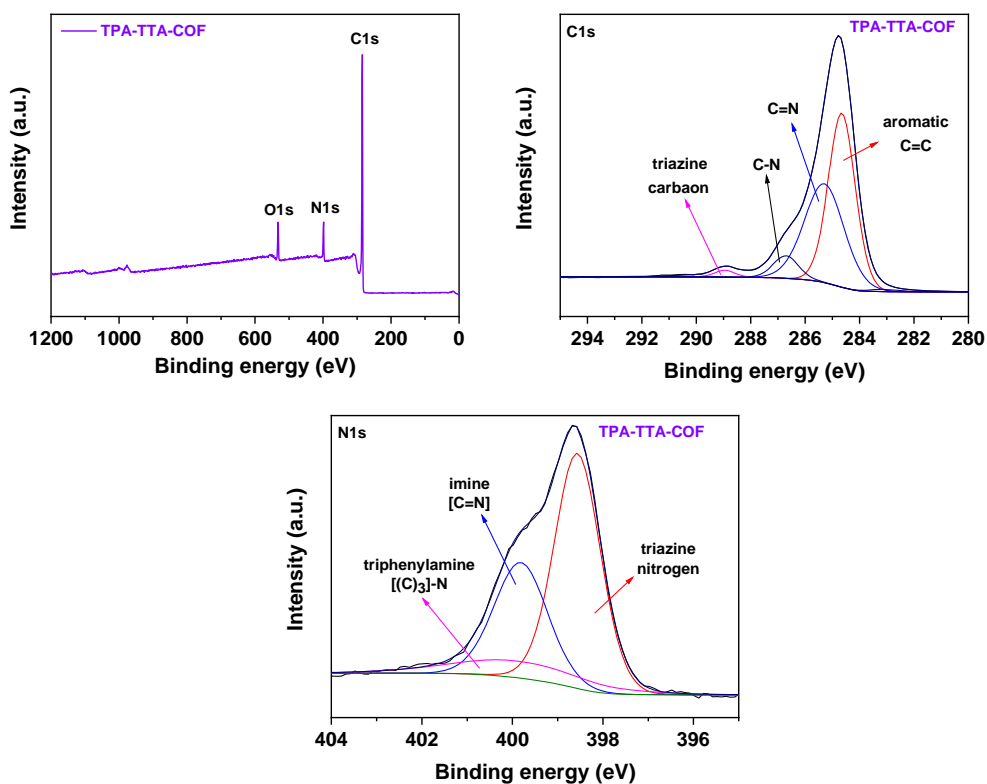


Fig. S16 XPS spectra of TPA-TTA-COF. No metal species was detected in the XPS survey spectra.

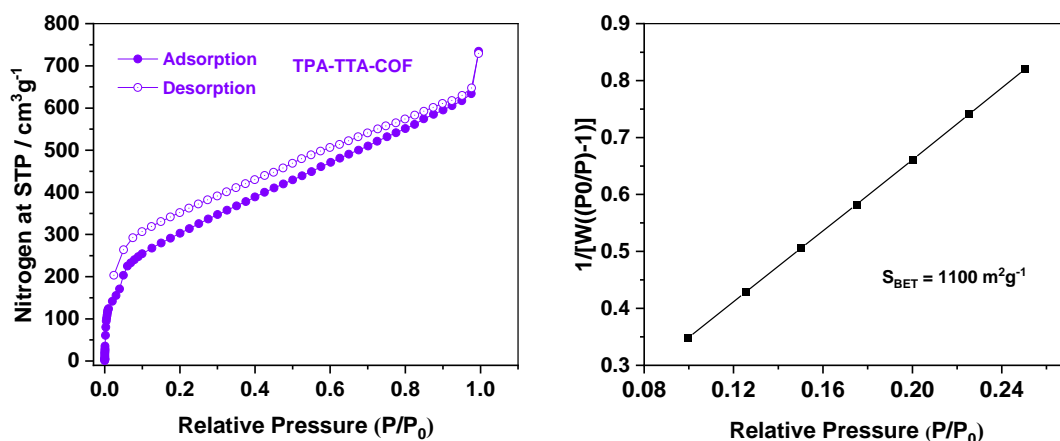


Fig. S17 Nitrogen sorption isotherm at 77K (left) and BET specific surface area plot (right) for TPA-TTA-COF. The BET surface area of TPA-TTA-COF is higher than that of PTZ-TTA-COF, which should be ascribed to the better crystallinity of TPA-TTA-COF than PTZ-TTA-COF.

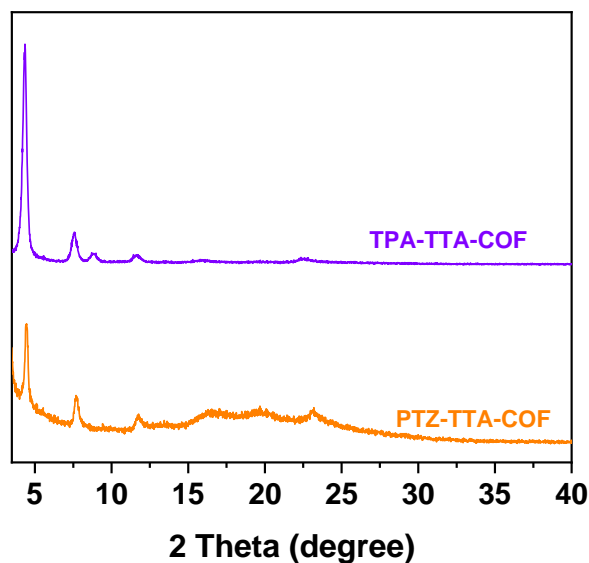


Fig. S18 The PXRD comparison of PTZ-TTA-COF with TPA-TTA-COF in the same scale. It can be found that TPA-TTA-COF exhibited some better crystallinity than that of PTZ-TTA-COF. This phenomenon should be attributed to the flexible butterfly-shaped configuration of PTZ unit, thus, impeding the facile crystallization of PTZ-based COF to some extent.

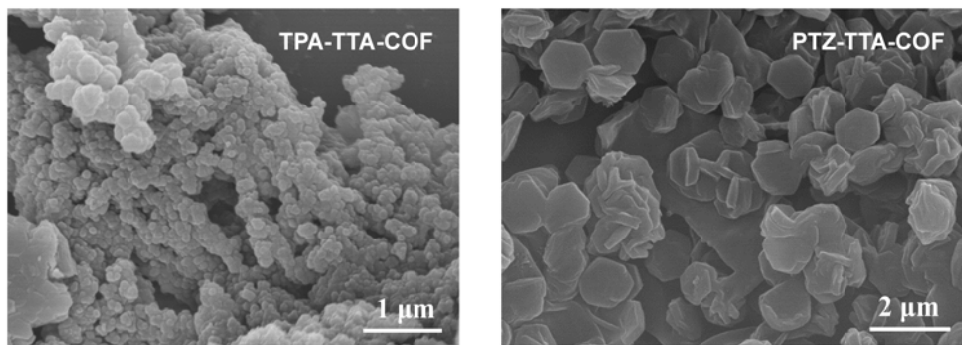


Fig. S19 The SEM comparison of TPA-TTA-COF and PTZ-TTA-COF, showing the particle size of TPA-TTA-COF is much smaller than that of PTZ-TTA-COF.

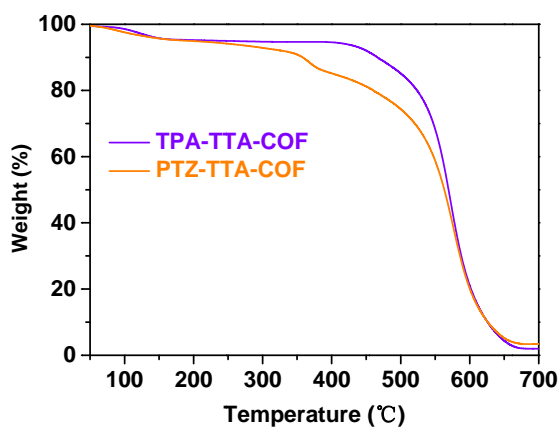


Fig. S20 TGA of PTZ-TTA-COF and TPA-TTA-COF under N_2 atmosphere with a heating rate of $10\text{ }^\circ\text{C}/\text{min}$. It can be found that TPA-TTA-COF exhibited a little better thermo-stability than that of PTZ-TTA-COF.

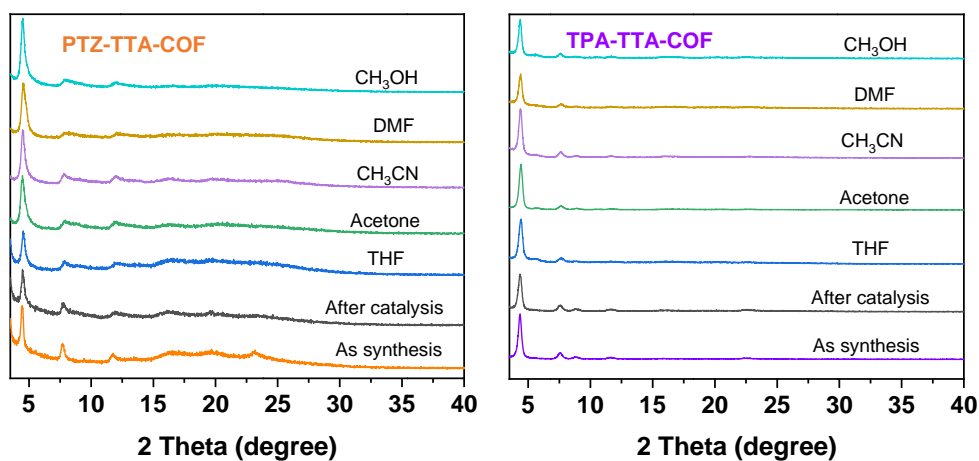


Fig. S21 PXRD patterns of PTZ-TTA-COF and TPA-TTA-COF (as-synthesized, after photocatalysis, as well as soaked in various organic solvent for 12h), revealing their framework stabilities.

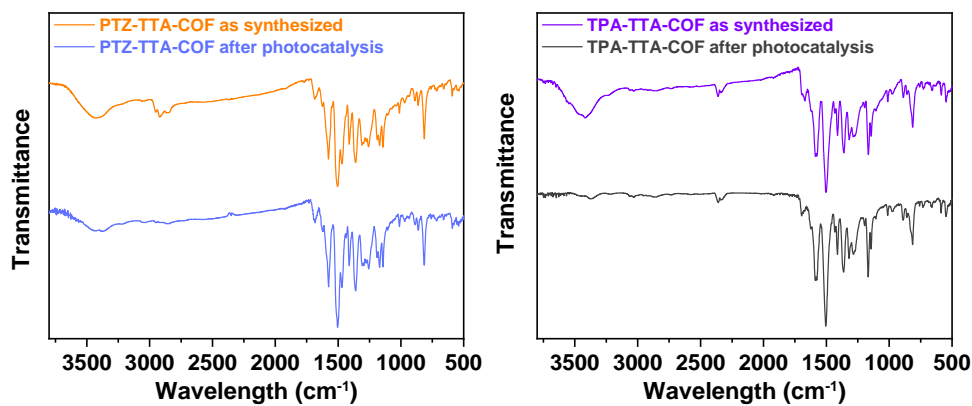


Fig. S22 FT-IR spectra of PTZ-TTA-COF and TPA-TTA-COF as-synthesized and after photocatalysis, indicating their chemical structural stability after photocatalysis.

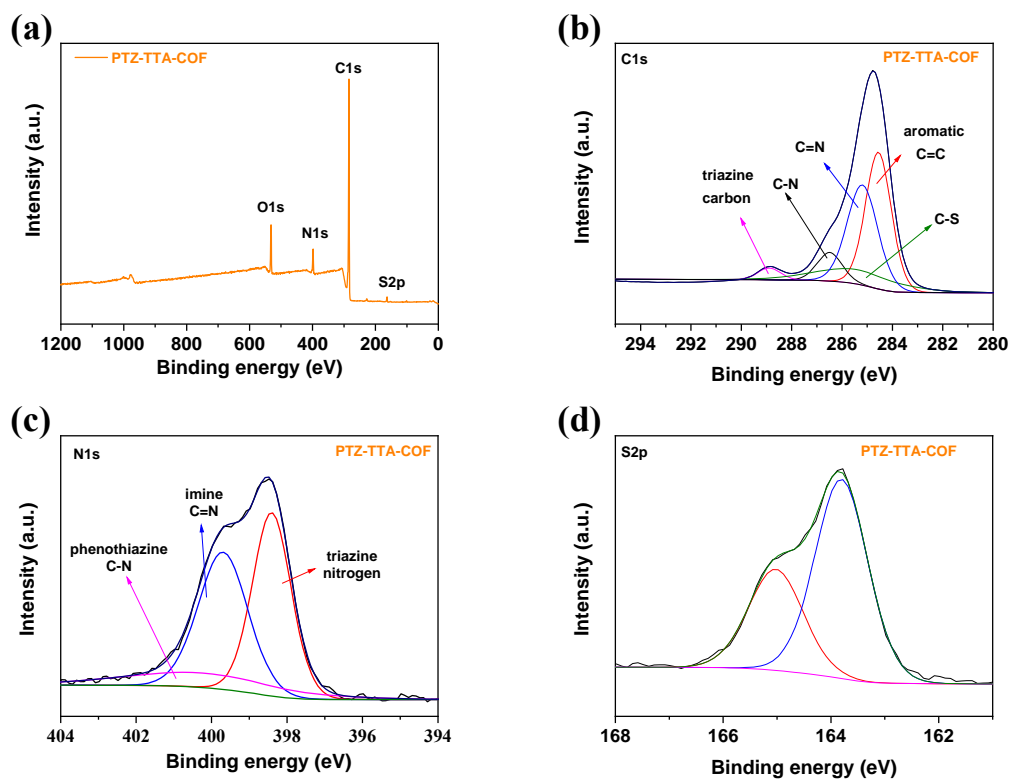


Fig. S23 XPS spectra of PTZ-TTA-COF. No metal species was detected in the XPS survey spectra.

Table S2. Atomistic coordinates for the refined unit cell parameters of PTZ-TTA-COF (AA stacking mode) optimized via Pawley refinement.

Molecular modeling of PTZ-TTA-COF was generated with the BIOVIA Materials Studio 7.0. Pawley refinement was carried out using Reflex, a software package for crystal determination from PXRD pattern. Unit cell dimension was set to the theoretical parameters. The Pawley refinement was performed to optimize the lattice parameters iteratively until the Rwp value converges and the overlay of the observed with refined profiles shows good agreement. The lattice models (e.g., cell parameters, atomic positions, and total energies) were then fully optimized using MS Forcite molecular dynamics module (universal force fields, Ewald summations) method.

Space-group P 1 - triclinic

$a = 23.4920 \text{ \AA}, b = 23.2820 \text{ \AA}, c = 3.6845 \text{ \AA}$

$\alpha = 92.2280^\circ, \beta = 103.0540^\circ, \gamma = 120.2430^\circ$

$V = 1667.81 \text{ \AA}^3 R_{wp} = 7.61\%, R_p = 5.91\%$

Atom	x/a	y/b	z/c	Atom	x/a	y/b	z/c
N1	0.5824	0.6841	0.6357	C39	0.0133	0.6143	0.6311
C2	0.6119	0.6437	0.6202	C40	-0.0251	0.5454	0.6185
C3	0.6838	0.6753	0.7074	C41	-0.0936	0.5146	0.6135
C4	0.7142	0.6372	0.697	C42	-0.1246	0.5525	0.6219
C5	0.6731	0.5669	0.6018	C43	-0.0861	0.6216	0.6353
C6	0.6011	0.5352	0.5161	C44	-0.0176	0.6524	0.6402
C7	0.5706	0.5733	0.524	C45	0.7053	0.5267	0.5965
C8	0.5685	1.1071	0.6859	C46	-0.1972	0.52	0.6126
C9	0.525	1.0349	0.6642	N47	0.7726	0.5566	0.6133
C10	0.4535	0.9995	0.4628	C48	0.6982	1.4226	0.584
C11	0.4136	0.9307	0.4433	N49	0.7655	1.453	0.6007
C12	0.4436	0.8957	0.6254	N50	0.6682	1.4596	0.5795
C13	0.5161	0.9318	0.8221	H51	0.7179	0.7324	0.7875
C14	0.5559	1.0008	0.8414	H52	0.7728	0.6632	0.7662

N15	0.401	0.8243	0.607	H53	0.567	0.478	0.4396
C16	0.4311	0.7837	0.5824	H54	0.5119	0.547	0.4519
C17	0.5024	0.8093	0.7744	H55	0.6275	1.1335	0.8149
S18	0.562	0.8934	1.0602	H56	0.4279	1.0268	0.3146
C19	0.3898	0.7176	0.3621	H57	0.3554	0.9016	0.2768
C20	0.4175	0.6774	0.3399	H58	0.6142	1.0292	1.0048
C21	0.4877	0.7028	0.5353	H59	0.3323	0.6957	0.1966
C22	0.5299	0.7688	0.7514	H60	0.3827	0.6238	0.1619
C23	0.516	0.66	0.5083	H61	0.5874	0.7894	0.9101
C24	0.3299	0.7941	0.6124	H62	0.4783	0.6043	0.3718
C25	0.289	0.7252	0.6063	H63	0.311	0.6916	0.5949
C26	0.2214	0.6964	0.6139	H64	0.1894	0.6404	0.606
C27	0.1929	0.7362	0.631	H65	0.21	0.8376	0.6589
C28	0.2327	0.8047	0.6429	H66	0.3316	0.8894	0.6481
C29	0.3003	0.8331	0.6353	H67	0.0996	0.7408	0.6446
N30	0.0831	0.6442	0.6298	H68	0.4892	1.2209	0.4125
N31	0.5412	1.142	0.5605	H69	0.5583	1.3453	0.4254
C32	0.1219	0.7074	0.6356	H70	0.7505	1.3412	0.726
C33	0.5816	1.2122	0.5686	H71	0.6819	1.2173	0.722
C34	0.548	1.2478	0.4853	H72	-0.0005	0.514	0.6121
C35	0.586	1.3164	0.4907	H73	-0.1247	0.4584	0.6026
C36	0.6582	1.3502	0.576	H74	-0.1106	0.653	0.6422
C37	0.6919	1.3144	0.6572	H75	0.0133	0.7086	0.6516
C38	0.654	1.2459	0.6544				

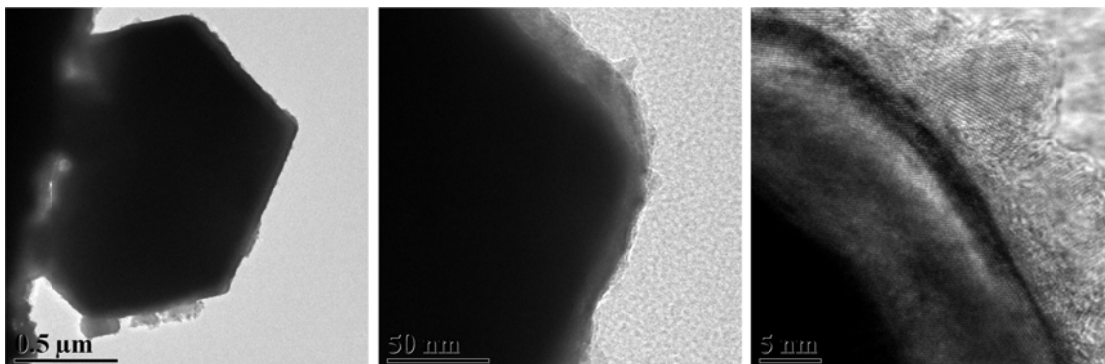


Fig. S24 TEM images of PTZ-TTA-COF with increasing amplification.

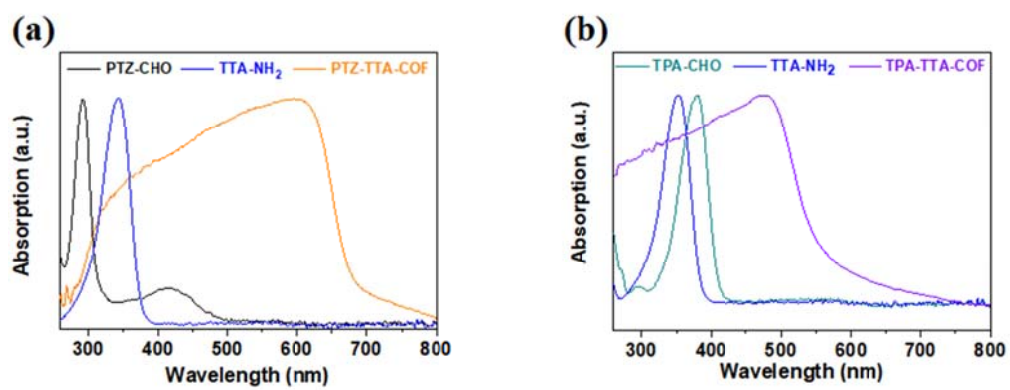


Fig. S25 UV-Vis spectra of (a) PTZ-TTA-COF, (b) TPA-TTA-COF, and their corresponding monomers.

Computational Methods:

All the density functional theory (DFT) calculations are carried out in the Vienna *Ab-initio* Simulation Package (VASP),^{S5} and VASPKIT^{S6} is used to post-process the data calculated by VASP. The generalized gradient approximation (GGA) is used with Perdew-Burke-Ernzerhof (PBE)^{S7,S8} exchange-correlation functional. The Projector augmented-wave (PAW) method is used to deal with the core electrons, and the valence electrons are described by a plane wave basis set with a cutoff energy of 450 eV. The adsorption energy and electronic properties are calculated by k-point grid (7×1×1). The convergence criteria of force and energy are set to 0.03eV·Å⁻¹ and 10⁻⁵eV, respectively. In order to obtain a better description of band gap, HSE06 hybrid functional^{S9} was used to calculate band structure. The path connected high-symmetry points in Brillouin zone were selected as Γ , M, K and Γ points and 60 K-points were sampled between each high-symmetry points. Density of states was also evaluated at HSE06 level with a denser Brillouin sampling of 12×12×1.

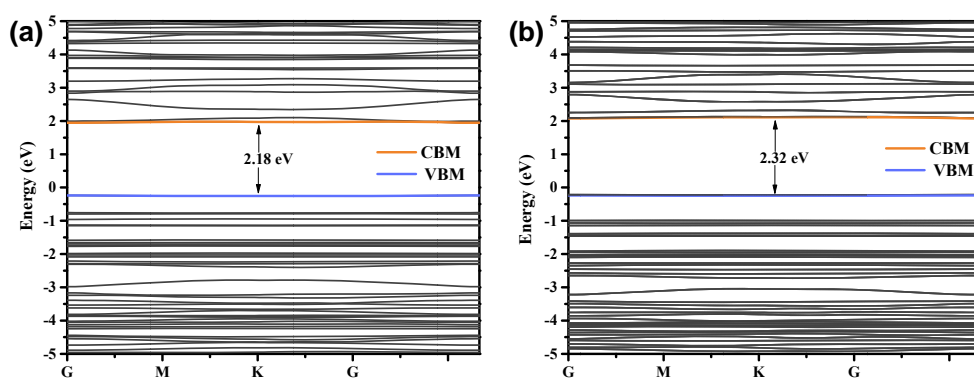


Fig. S26 Calculated electronic band structures of PTZ-TTA-COF (a) and TPA-TTA-COF (b) by the screened hybrid functional method HSE06.

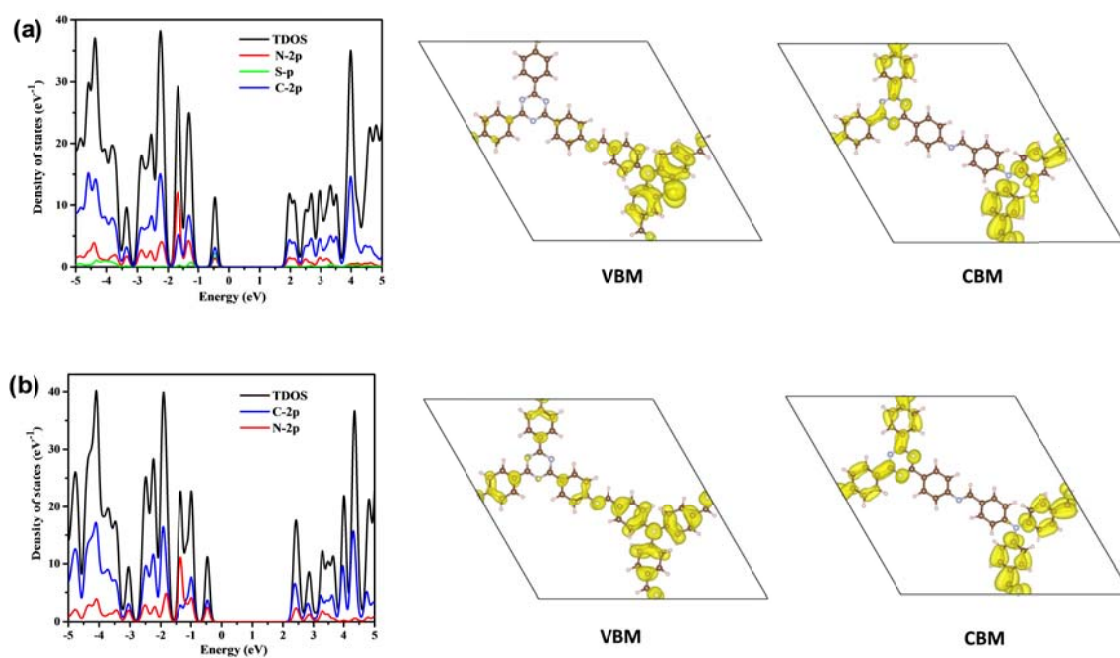


Fig. S27 The calculated total and partial densities of states (DOS) projected on atomic orbitals as well as spatial charge distributions of VBM and CBM for PTZ-TTA-COF (a) and TPA-TTA-COF (b).

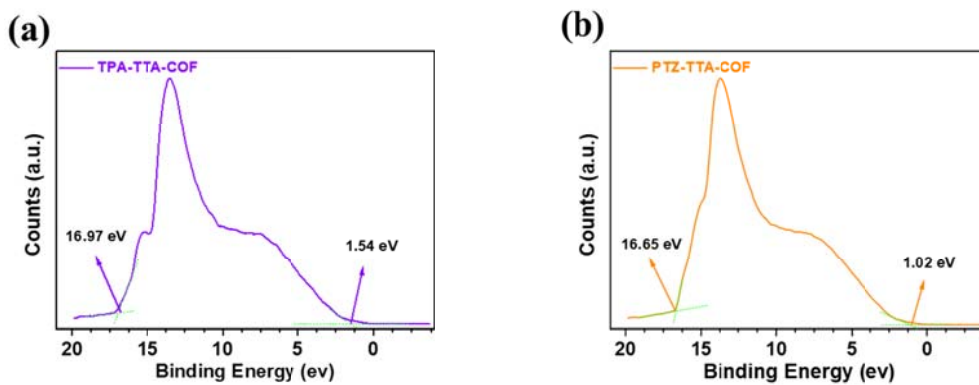


Fig. S28 High-resolution valence band ultraviolet photoelectron spectra (UPS) of TPA-TTA-COF (a) and PTZ-TTA-COF (b).

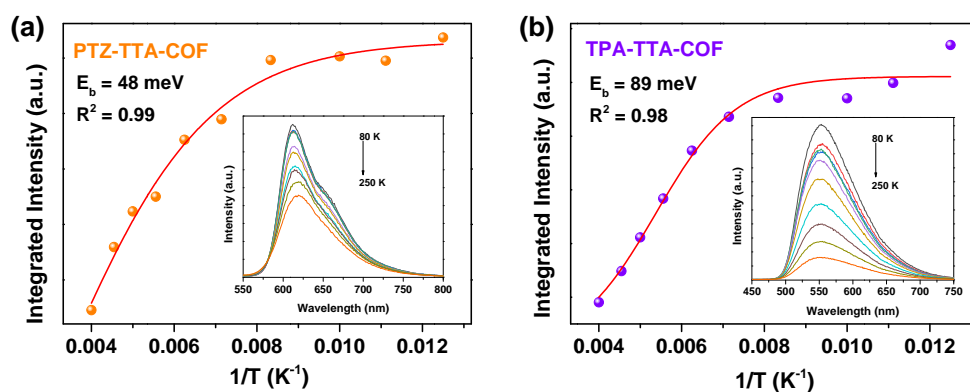


Fig. S29 Integrated PL intensity of PTZ-TTA-COF (a) and TPA-TTA-COF (b) as a function of temperature (inset: their corresponding temperature-dependent PL spectra from 80 to 250 K).

Arrhenius equation for fitting PL data:

$$I(T) = \frac{I_0}{1 + Ae^{-E_b/k_B T}}$$

I_0 is the intensity at 0 K, A is a proportional constant and k_B is the Boltzmann constant, E_b is the exciton binding energy.

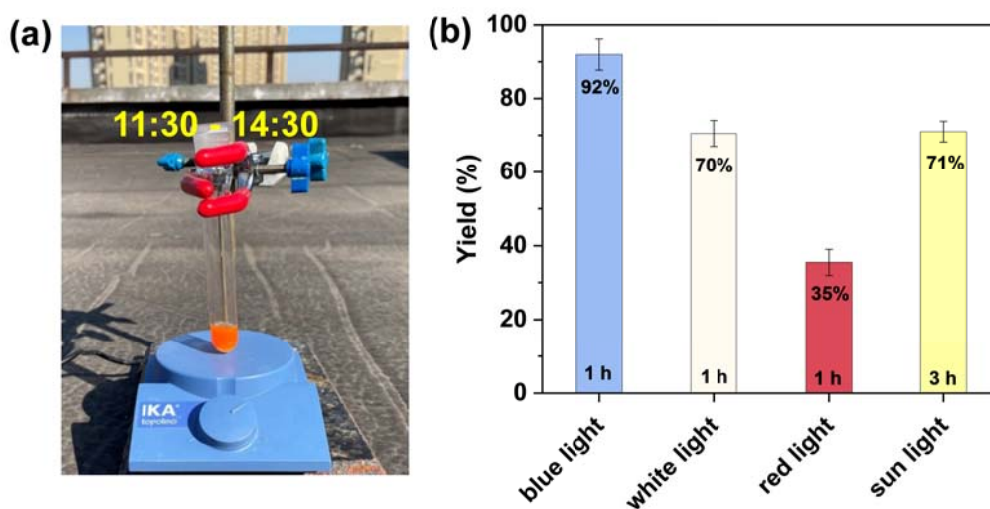


Fig. S30 (a) The simple setup for natural sunlight driven the photocatalytic model reaction of benzylamine to its imine by PTZ-TTA-COF for 3 h; (b) Yields of the photocatalytic model reaction of benzylamine to its imine by PTZ-TTA-COF under different light sources. Reaction conditions: benzylamine (0.1 mmol), PTZ-TTA-COF (2 mg), solvent acetonitrile (CD_3CN , 1 mL), 1 h, in the open air at room temperature. The yields were determined by ^1H NMR.

The model reaction of PTZ-TTA-COF photocatalyzed oxidative coupling of benzylamine to its imine was further performed by using different light sources, including natural sunlight, white LEDs, and red LEDs. The corresponding yields were summarized in **Fig. S30**. Due to the broad light absorption range of PTZ-TTA-COF, this photocatalytic model reaction can occur with various yields under the different light irradiation. Besides, it can be found that blue LEDs gave the best yield of 92% because of the highest energy of blue light, while the lowest yield of 35% was obtained under red LEDs due to the lowest energy of red light. On the other hand, this reaction also can go well under the natural sunlight (71%, for 3 h at noon in October. *However, the activity is not high, which may be ascribed to the weak sunlight in autumn.*).

Table S3. The comparison of photocatalytic oxidative cyclization of five thioamides to 1,2,4-thiadiazoles by PTZ-TTA-COF and TPA-TTA-COF.^a

Entry	Substrate	Product	Time (h)	Yield ^b (%)
1			2	72 ^c
				33 ^d
2			2	61 ^c
				37 ^d
3			2	72 ^c
				34 ^d
4			2	60 ^c
				25 ^d
5			2	67 ^c
				26 ^d

^aReaction conditions: thioamide (0.05 mmol), COF (2 mg), CH₃CN (1 mL), irradiation with blue LEDs ($\lambda_{\text{max}} = 450 \text{ nm}$, 3 W \times 4), 2 h. ^bdetermined by ¹H NMR analysis. ^cby PTZ-TTA-COF. ^dby TPA-TTA-COF.

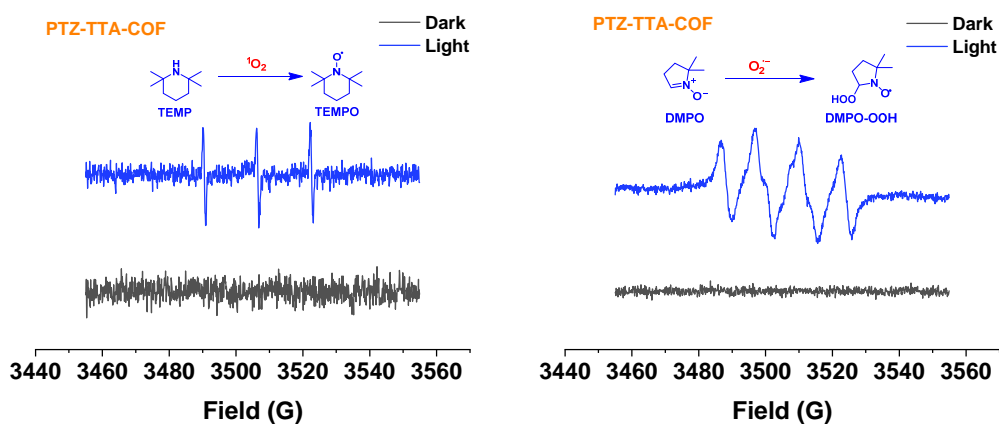


Fig. S31 EPR spectra of a mixture of PTZ-TTA-COF with TEMP upon light irradiation and in the dark (left) as well as DMPO upon light irradiation and in the dark (right).

Determination for the generation of ammonia in photocatalytic oxidative coupling reaction of amines:

Benzylamine (0.1 mmol) and PTZ-TTA-COF (2 mg) was mixed in acetonitrile (1 mL), which was stirred and irradiated by blue LEDs for 1 h at room temperature in air. Then, COF sample was separated from the reaction mixture by high speed centrifugation. After that, 2 mL DI water was added into the above solution, which subsequently was extracted by 5 mL dichloromethane for twice. The aqueous layer was subject to pH test, showing its basic solution (pH = 8-9, **Fig. S32a**). In order to rule out other possible factor caused pH change, two control experiments were further performed as the same above procedure but without benzylamine or light irradiation, respectively. It can be found that both of the two aqueous layers were neutral with pH = 6-7 (**Fig. S32b** and **S32c**). Based on these experimental results, the pH change of (a) solution should be derived from ammonia. Thus, we can conclude that ammonia was produced in the photocatalytic oxidative coupling reaction of amines.

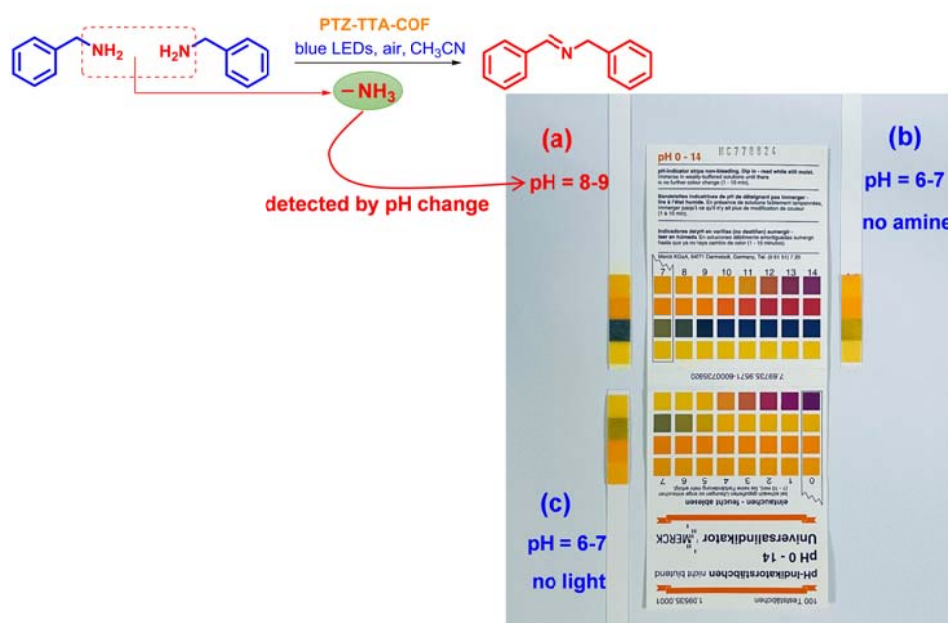


Fig.S32 The pH test after the photocatalytic oxidative coupling of benzylamine to its imine (a), and two control experimental results (b and c).

Determining the limiting step in photocatalytic oxidative coupling reaction of amines:

Table S4 PTZ-TTA-COF photocatalyzed oxidative coupling of benzylamine to its imine under various conditions.^a

Entry	PTZ-TTA-COF	Benzylamine	Time	Atmosphere	Product Yield
1	1 mg	0.1 mmol	30 min	air	52
2	2 mg	0.1 mmol	30 min	air	72
3	3 mg	0.1 mmol	30 min	air	71
4	2 mg	0.1 mmol	30 min	O ₂	97
5	2 mg	0.2 mmol	30 min	air	44
6	2 mg	0.3 mmol	30 min	air	29

^aReaction conditions: CD₃CN (1 mL), blue LEDs (λ_{\max} = 450 nm, 3 W x 4), at room temperature. The yields were determined by ¹H NMR.

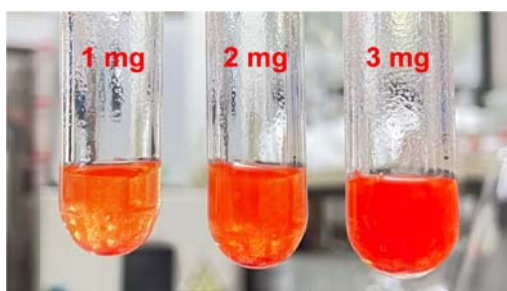


Fig. S33 Different weight of PTZ-TTA-COF samples were dispersed into 1 mL acetonitrile.

First, a different amount of PTZ-TTA-COF was used to photocatalyze the reaction for 30 min (Entry 1-3, **Table S4**). The highest yield was obtained when using 2 mg COF sample. In contrast, a relatively decreased yield was observed for the case of 3 mg COF sample (*when considering the higher weight of 3 mg COF photocatalyst than 2 mg*), which should be ascribed to its too high concentration. From the comparison of different COF concentration in **Fig. S33**, it can be found that light is difficult to penetrate the mixture solution (3 mg/mL). As a result, the COF

photocatalyst in the inner solution cannot be efficiently excited. Additionally, too high concentration of photocatalyst often results in the self-quenching of exciton, thus, decreasing its photocatalytic activity. Based on these results, the suitable concentration of COF was determined to be 2 mg/mL in acetonitrile.

Second, when the reaction was conducted in pure O₂ atmosphere (Entry 4, **Table S4**), the rate is obviously accelerated in comparison to air atmosphere, whereas only trace product was detected in N₂ atmosphere. This result indicated that oxygen played a critical role in this photocatalytic process. Besides, we also employed quenching experiments and EPR measurements to identify the reactive oxygen species (ROS) of ¹O₂ and O₂^{•-}, which were generated by the electron and energy transfer process from excited COF photocatalyst to O₂ molecules.

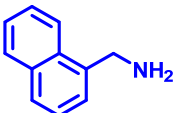
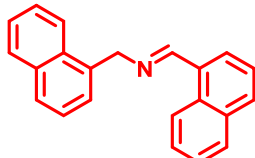
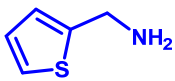
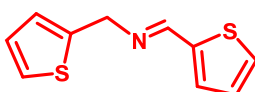
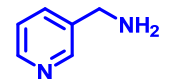
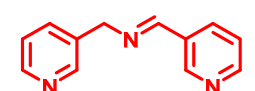
Third, we further investigated the reaction under the different concentration of benzylamine. It was found that when the substrate concentration was increased from 0.1 mmol to 0.2 and 0.3 mmol (Entry 5 and 6, **Table S4**), the product yield was decreased to be 44% and 29%, respectively. This result demonstrated that the conversion of benzylamine was determined by the generation rate of ROS in the mixture solution.

Based on these above results and the proposed mechanism, it is reasonable to speculate that the limiting step in this photocatalytic reaction should be the ROS generation produced by the electron and energy transfer process from photo excited PTZ-TTA-COF to O₂ molecules.

Table S5. Photocatalytic oxidative coupling of various amines by **PTZ-TTA-COF**^a



Entry	Substrate	Product	Time (h)	Yield ^b (%)
1			1	92
2			1	96
3			1	99
4			1	96
5			2	97
6			1	91
7			1	95
8			1	95
9			1	75
10			1	84
11			2	91

12			2	99
13			2	99
14			2	85

^aReaction conditions: benzylamines (0.1 mmol), PTZ-TTA-COF (2 mg), CD₃CN (1 mL), irradiation with blue LEDs ($\lambda_{\text{max}} = 450 \text{ nm}$, 3 W \times 4), 1 h. ^bDetermined by ¹H NMR analysis.

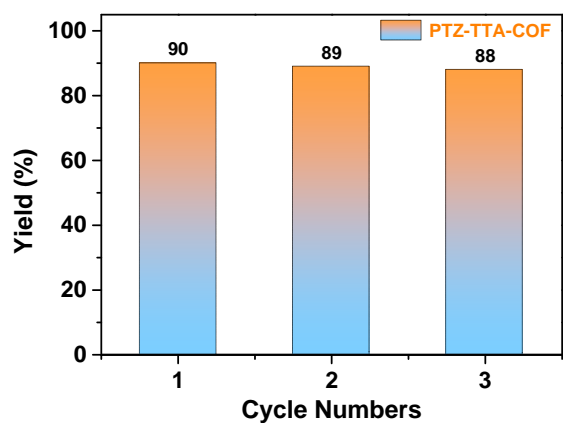


Fig. S34 Recycling of PTZ-TTA-COF for the photocatalyzed aerobic oxidative coupling of benzylamine to imine.

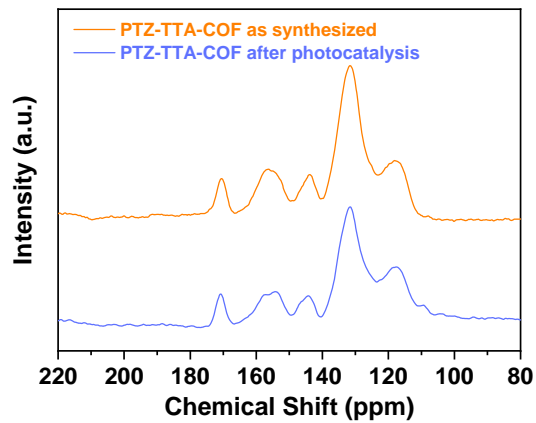


Fig. S35 Solid-state ^{13}C NMR of PTZ-TTA-COF as-synthesized (orange) and after photocatalysis (blue).

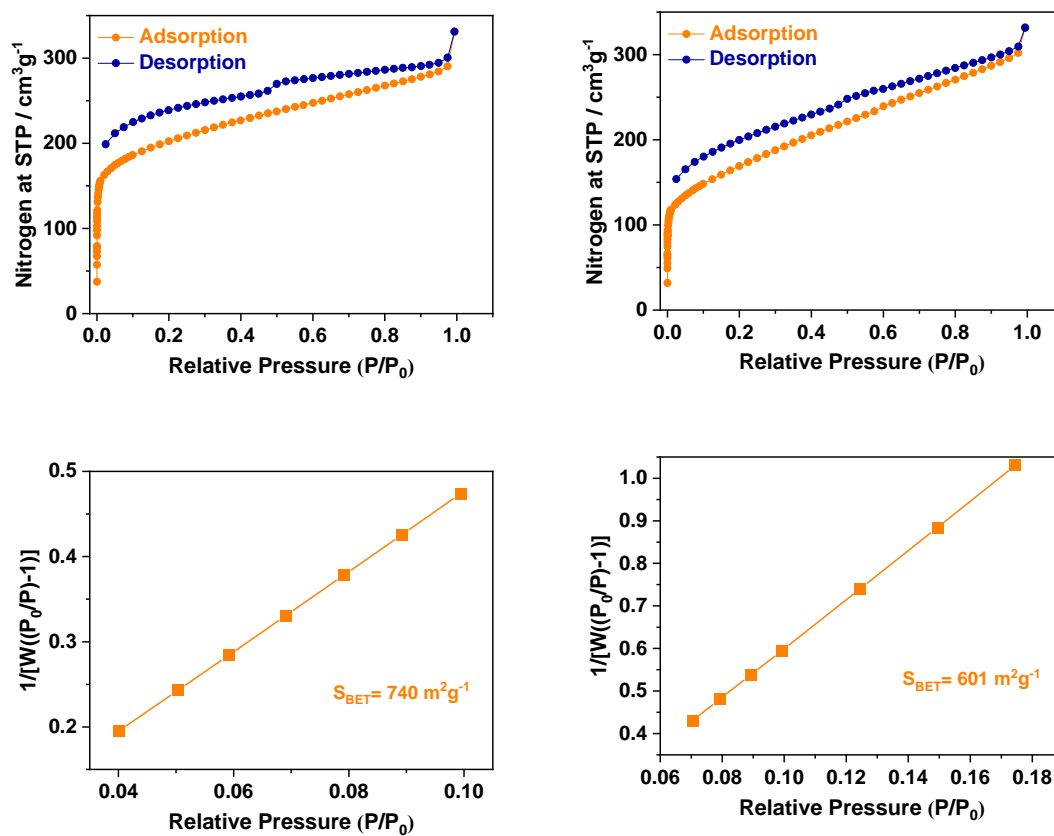


Fig. S36 Nitrogen sorption isotherms for PTZ-TTA-COF as-synthesized (left) and after photocatalysis (right).

References

- S1. A. Halder, S. Kandambeth, B. P. Biswal, G. Kaur, N. C. Roy, M. Addicoat, J. K. Salunke, S. Banerjee, K. Vanka, T. Heine, S. Verma and R. Banerjee, *Angew. Chem. Int. Ed.*, 2016, **55**, 7806-7810.
- S2. R. Luo, H. Lv, Q. Liao, N. Wang, J. Yang, Y. Li, K. Xi, X. Wu, H. Ju and J. Lei, *Nat. Commun.*, 2021, **12**, 6808.
- S3. J. Yang, A. Acharjya, M.-Y. Ye, J. Rabeah, S. Li, Z. Kochovski, S. Youk, J. Roeser, J. Grüneberg, C. Penschke, M. Schwarze, T. Wang, Y. Lu, R. van de Krol, M. Oschatz, R. Schomäcker, P. Saalfrank and A. Thomas, *Angew. Chem. Int. Ed.*, 2021, **60**, 19797-19803.
- S4. S. Wang, Y. Yang, H. Zhang, Z. Zhang, C. Zhang, X. Huang, D. Kozawa, P. Liu, B.-G. Li and W.-J. Wang, *J. Am. Chem. Soc.*, 2021, **143**, 5003-5010.
- S5. G. Kresse and J. Furthmüller, *Phys. Rev. B*, 1996, **54**, 11169-11186.
- S6. V. Wang, N. Xu, J.-C. Liu, G. Tang and W.-T. Geng, *Comput. Phys. Commun.*, 2021, **267**, 108033.
- S7. J. P. Perdew, K. Burke and M. Ernzerhof, *Phys. Rev. Lett.*, 1996, **77**, 3865-3868.
- S8. J. P. Perdew, K. Burke and M. Ernzerhof, *Phys. Rev. Lett.*, 1997, **78**, 1396-1396.
- S9. A. V. Krukau, O. A. Vydrov, A. F. Izmaylov and G. E. Scuseria, *J. Chem. Phys.*, 2006, **125**, 224106.